Research Article | Vol. 27, No. 16 | 5 Aug 2019 | OPTICS EXPRESS 22685
Optics EXPRESS

Implementation of artifact-free circular dichroism SHG imaging of collagen

MARGAUX SCHMELTZ,[1] CLAIRE TEULON,[1] GAËL LATOUR,[2] DJIDA GHOUBAY,[3] VINCENT BORDERIE,[3] CAROLE AIMÉ,[4] AND MARIE-CLAIRE SCHANNE-KLEIN[1,*]

[1]*LOB, École polytechnique, CNRS, Inserm, IP Paris, F-91128 Palaiseau, France*
[2]*Laboratoire IMNC, Université Paris-Sud, CNRS, Université Paris-Saclay, F-91405 Orsay, France*
[3]*Sorbonne Université, CHNO des Quinze Vingt, INSERM, Institut de la Vision, GRC32, CIC1423, F-75012 Paris, France*
[4]*Sorbonne Université, CNRS, LCMCP, Paris, F-75005, France*
[*]*marie-claire.schanne-klein@polytechnique.edu*

Abstract: Second harmonic generation (SHG) enables *in situ* imaging of fibrillar collagen architecture in connective tissues. Recently, Circular Dichroism SHG (CD-SHG) microscopy has been implemented to take advantage of collagen chirality to improve 3D visualization. It measures the normalized difference in the SHG signal obtained upon excitation by left versus right circular polarizations. However, CD-SHG signal is not well characterized yet, and quite different CD-SHG values are reported in the literature. Here, we identify two major artifacts that may occur in CD-SHG experiments and we demonstrate that thorough optimization and calibration of the experimental setup are required for CD-SHG imaging. Notably it requires a careful calibration of the incident circular polarizations and a perfect mechanical stabilization of the microscope stage. Finally, we successfully record CD-SHG images in human cornea sections and confirm that this technique efficiently reveals collagen fibrils oriented out of the focal plane.

1. Introduction

Collagen is a major structural protein in vertebrates, as it is the main component of connective tissues, such as arteries, tendons, skin, bones or cornea. In fibrillar collagen types, collagen triple helices self-assemble into fibrils that exhibit various sizes and form various 3D structures depending on the observed tissue [1]. For example in cornea, type I collagen 30 nm-thick fibrils align in ~2 µm-thick lamellae that are stacked with different en-face orientations along the stroma depth, while fibrils in tendon assemble to form few µm-diameter fibers that further assemble into larger fascicles. These 3D structures provide physical and mechanical properties to the observed connective tissues [2]: transparency and rigidity to cornea, mechanical strength to tendon. A change of collagen 3D organization or a defect in collagen synthesis can lead to pathologies or tissue dysfunctions [3]. *In situ* imaging of these 3D structures is therefore a major biomedical concern, in particular to characterize pathological remodeling of connective tissues and to guide tissue bio-engineering.

Nowadays, the gold standard technique for *in situ* 3D visualization of collagen fibrils in intact tissues is second harmonic generation (SHG) microscopy [4,5]. This technique can be completed by additional modalities as Polarization-resolved (P-SHG) or interferometric (I-SHG) measurements. P-SHG provides information about the hierarchical organization of collagen: mainly the mean orientation of collagen fibrils and their degree of alignment within the focal volume, and the triple helix molecular structure in tissues with well-aligned fibrils [6–13]. I-SHG provides the relative phase of the SHG signal and gives information about the polarity of collagen fibrils in the focal plane [14–16]. However, P-SHG and I-SHG only provide information about orientation and polarity within the focal plane. Together with regular SHG imaging, P-SHG and

#370384 https://doi.org/10.1364/OE.27.022686
Journal © 2019 Received 20 Jun 2019; revised 17 Jul 2019; accepted 18 Jul 2019; published 24 Jul 2019

Optics EXPRESS

I-SHG are thus powerful techniques to probe in-plane collagen architecture, but they are poorly sensitive to structures lying out of the focal plane. This may impede the determination of the collagen 3D organization in dense collagen tissues, where 3D or transverse reconstructions are often ambiguous.

Recently, circular dichroism SHG microscopy (CD-SHG) was reported to highlight out-of-plane collagen structures [17, 18]. CD-SHG measures the normalized difference in the SHG signal obtained upon excitation by left versus right circular polarizations and is related to the chirality of collagen at molecular and tissular scales. It was first implemented in surface SHG experiments on various chiral molecules [19, 20], including collagen [21], and has expanded to microscopy measurements on biological samples since 2012 [17, 18, 22–24]. However, the CD-SHG signal is not well characterized yet. First, CD-SHG measurements reported in the literature show highly different values: between 5 % to nearly 100 % depending on the studied tissue [17, 22]. Then, as the SHG signal is known to decrease while the out-of-plane angle increases, CD-SHG involves the difference between two low SHG signals. It is therefore quite sensitive to noise and deserves proper computation of the measurement accuracy. In addition, CD-SHG imaging requires perfect circular incident polarizations, which are difficult to obtain and are easily affected along propagation.

In this study, different artifacts affecting CD-SHG imaging are identified and reported. We first show that imperfect circular incident polarizations lead to linear dichroism contribution to the CD-SHG signal and result in a misinterpretation of CD-SHG images. We then assess the accuracy of CD-SHG signal and show that time-lapse acquisitions are required to improve the measurement accuracy. We also demonstrate that a slight movement in the microscope stage or in the sample during these acquisitions leads to artifactual features in the CD-SHG images. Finally, an artifact-free circular dichroism SHG imaging of human cornea transverse sections is presented, highlighting the out-of-plane collagen structures of this tissue.

2. Materials and methods

2.1. Sample preparation

Three sample types were used for this study: tendons as a standard easy-to-handle collagen sample, corneas because of their complex 3D architecture and collagen membranes that provided large homogeneously structured areas. No distortion of polarization was expected upon propagation in all these thin samples.

The study was carried out according to the tenets of the Declaration of Helsinki and followed ethical requirements for human tissues. We obtained human corneas (n=4) from the French Eye Bank (Banque Française des Yeux, Paris), which were unsuitable for transplantation and assigned to scientific use. They were fixed in 2.5 % glutaraldehyde in 0.1 M cacodylate buffer (pH 7.4), postfixed in 1 % osmium tetraoxide in 0.2 M cacodylate buffer (pH 7.4), included in epoxy resin and cut with an ultramicrotome. Other human corneas (n=4) featuring the same qualification criteria were obtained from another eye bank (Établissement Français du Sang, Paris). They were fixed in 4 % PFA, immersed in a 30 % sucrose solution, embedded in Tissue-Tex O.C.T. compound and cooled to -20°C, before cryostat sectioning. All sections were semi-thin transverse sections (3 - 6 µm-thick).

Series of tendons were dissected from 2 rat tails. The fascicles were rinsed and stored at 4° in phosphate-buffered saline (PBS), and used within a few days for the experiments. They were deposited and flattened on a coverslip with PBS and covered with another coverslip.

Fibrillar collagen membranes were made from type I collagen that was extracted and purified from rat tail tendons by substituting 500 mM acetic acid by 3 mM hydrochloric acid as previously described in [25]. Collagen purity was assessed by electrophoresis and its concentration estimated by hydroxyproline titration [26]. Then, 1.2 mL of collagen solution at a concentration of 1.7 $mg.ml^{-1}$ in 30 mM HCl and 75 % vol. ethanol, or alternatively in 30 mM HCl only, was poured in

Optics EXPRESS

a silicon mold to obtain casted collagen membranes after an overnight solvent evaporation under ambient conditions. These ~50 µm-thick membranes were imaged between two 170 µm-thick glass coverslips.

2.2. SHG microscopy

A custom-built laser scanning upright microscope was used to perform SHG imaging [27]. The excitation source was a femtosecond titanium:sapphire laser (MaiTai, SpectraPhysics) tuned to 860 nm and delivering pulses around 100 fs with a 80 MHz repetition rate. Laser power was controlled by the orientation of an achromatic half waveplate before a Glan prism, and was less than 10 mW at the sample, with 10 to 20 µs/pixel dwell time and 0.1 to 0.2 µm pixel size. A high numerical aperture objective with water immersion (25x, NA 1.05, Plan-Apochromat, Olympus) was used to achieve approximately 0.4 µm lateral by 1.2 µm axial resolutions near the sample surface. These experimental resolutions were measured from the two-photon excitation PSF obtained from 100 nm-diameter fluorescent micro-beads (Carboxylate-modified FluoSpheres beads, ThermoFisher Scientific) [28]. SHG signals were detected in the forward direction through a condenser (effective NA ≈ 1) using a photon-counting photomultiplier tube (P25PC, SensTech) and suitable spectral filters to reject the excitation laser beam (FF01-720/SP and FF01-680/SP, Semrock) and select SHG signals (FF01-427/10 interferential filter, Semrock).

2.3. Circular dichroism SHG measurements (CD-SHG)

The circular dichroism in SHG (CD-SHG) is measured as the normalized intensity difference between two SHG signals $I_R^{2\omega}$ and $I_L^{2\omega}$ obtained upon excitation with a right or left circular polarization respectively:

$$\text{CD-SHG} = \frac{I_L^{2\omega} - I_R^{2\omega}}{(I_L^{2\omega} + I_R^{2\omega})/2} \tag{1}$$

By definition [19, 20], this parameter belongs to the interval [-2,2], while CD in linear optics is in the interval [-1,1]. All CD-SHG images are presented with their scales specified, using a blue-white-red color chart. Experimentally, two images were recorded sequentially, using an incident right (RCP) or left (LCP) circular polarization respectively. Then the CD-SHG (normalized difference of the two images) and the average SHG intensity (average of the two images) were computed pixel-by-pixel. The mean background noise was around 0.1 photon in areas devoid of collagen, so the SHG signal was processed directly without any background subtraction.

The incident beam polarization was controlled by two motorized achromatic waveplates (Fichou, France) inserted at the back pupil of the objective. A first quarter waveplate improved the incoming beam linear polarization affected by galvanometric and dichroic mirrors to achieve a well-defined linear polarization. A second quarter waveplate was then positioned to achieve either right or left circular polarizations. A thorough protocol was used to measure and optimize the ellipticity of polarizations (defined as the ratio of the minimum to the maximum magnitudes of the incoming field vector) in the whole field of view. To that purpose, we used a powermeter (Nova II, Ophir) placed after a rotating analyzer (LPVIS100 and PRM1Z8, Thorlabs) to measure the incoming intensity at different angles α of the analyzer. The Malus's law allows us to fit the data by $I(\alpha) = y0 + A * cos^2(\alpha)$ and to calculate the ellipticity as:

$$e = \frac{E_{min}}{E_{max}} = \sqrt{\frac{I_{min}}{I_{max}}} = \sqrt{\frac{y_0}{y_0 + A}} \tag{2}$$

The position of the waveplates was then optimized by an iterative procedure so that the ellipticity tends to 1 (perfect circular polarization) for both right and left circular polarizations. This optimization was performed at the center of the field of view, and the ellipticity was then carefully measured at different pixels throughout the field of view.

Optics EXPRESS

3. Results and discussion

3.1. Elliptical incident polarizations lead to artifactual CD-SHG measurements

Right and left circular polarizations of the incident beam must be used to perform CD-SHG imaging. Nevertheless, perfect circular polarizations are rapidly distorted upon propagation. Most of the time, one ends up with a non perfect circular (elliptical) polarization, whose ellipticity is $e < 1$ (e is defined in Eq. 2). In this case, the electric field vector describes an ellipse. Setting $\vec{u}_1$ and $\vec{u}_2$ the unit vectors along respectively the major and the minor axes of the ellipse, the elliptically polarized incident beam is written as:

$$\vec{E_{ell}} = E_1 e^{i\phi}\vec{u}_1 + E_2 e^{i(\phi+\frac{\pi}{2})}\vec{u}_2 \tag{3}$$

with $E_2 \leq E_1$. This field can be seen as the sum of a circularly polarized field and a linearly polarized one:

$$\begin{aligned} \vec{E_{ell}} &= \sqrt{2}E_2 e^{i\phi} \times \left(\frac{1}{\sqrt{2}}\vec{u}_1 + \frac{i}{\sqrt{2}}\vec{u}_2\right) + (E_1 - E_2)e^{i\phi} \times \vec{u}_1 \\ &= \sqrt{E_1^2 + E_2^2} \times (p_1\vec{\varepsilon}_{circ} + p_2\vec{\varepsilon}_{lin}) \end{aligned} \tag{4}$$

where $p_1 = \frac{\sqrt{2}E_2}{\sqrt{E_1^2+E_2^2}}$ and $p_2 = \frac{E_1-E_2}{\sqrt{E_1^2+E_2^2}}$ are the weights of circular and linear polarizations in the overall elliptical polarization respectively, $\vec{\varepsilon}_{circ}$ is a circularly polarized field and $\vec{\varepsilon}_{lin}$ a linearly polarized field along $\vec{u}_1$. These two fields have their intensities normalized to 1.
The weights p_1 and p_2 can be expressed in terms of the ellipticity $e = \frac{E_2}{E_1}$:

$$\begin{aligned} p_1 &= \frac{\sqrt{2}e}{\sqrt{1+e^2}} \\ p_2 &= \frac{1-e}{\sqrt{1+e^2}} \end{aligned} \tag{5}$$

A perfectly circular polarization corresponds to an ellipticity $e = 1$, $p_1 = 1$ and $p_2 = 0$. However, a non-zero amount of linear polarization ($p_2 > 0$), either in the right or in the left incident polarization, affects the SHG measurement, because of linear incident field contribution. More precisely, as the second harmonic response scales as the square of the incident field, it involves here the squares of the circular and linear components of the incident field as well as cross-term between its linear and circular components. Consequently, the signal measured as "CD-SHG" is actually a combination of circular dichroism, linear dichroism (normalized difference in SHG signal upon an excitation linearly polarized along 2 perpendicular directions) and cross-terms mixing linear and circular contributions.

To characterize the effect of such a mix in CD-SHG signal, experiments were conducted with elliptical incident polarizations ($e \approx 0.2$) and quasi-perfect circular incident polarizations ($e \approx 0.97$) respectively, on samples rotated in the plane of the image (Fig. 1). For each case, CD-SHG images of a human cornea transverse section were measured before and after a 90°-in-plane rotation of the sample. In the case of elliptical incident polarizations, CD-SHG image of the cornea before rotation shows mainly a strong and positive signal (in red) within collagen fibrils oriented at 45° from the y-axis (Fig. 1(c)), whereas it shows a strong negative signal (in blue) after the 90°-in-plane rotation of the sample, where the fibrils are mainly at 135° from the y-axis (Fig. 1(d)). In contrast, in the case of quasi-perfect circular polarizations, no difference is observed in the CD-SHG signal before and after the in-plane rotation of the sample (Figs. 1(f) and 1(g)).

Optics EXPRESS

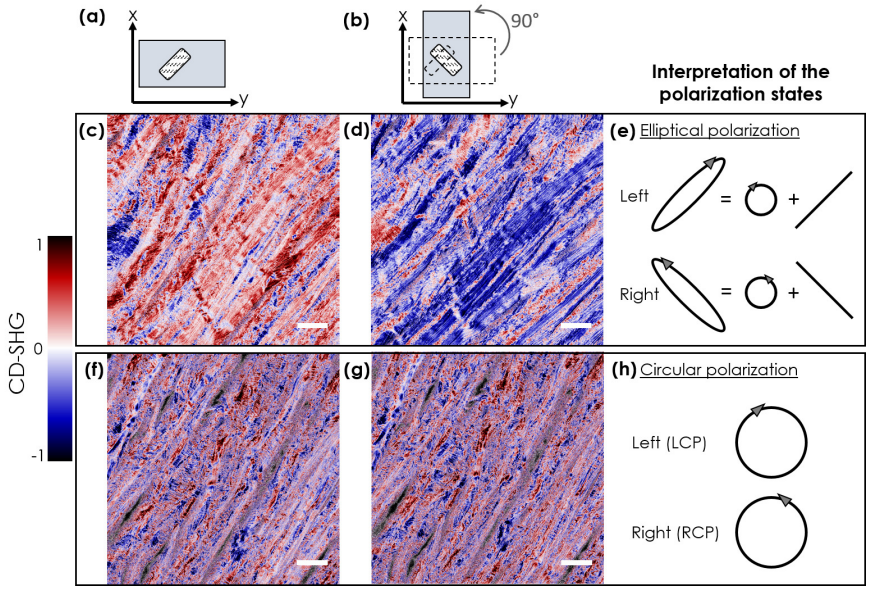

Fig. 1. Effect of the incident polarization ellipticity on CD-SHG measurements. (a) Top-view of the sample configuration for experiments depicted in (c) and (f). (b) Top-view of the sample in-plane rotation by +90° and new configuration for experiments depicted in (d) and (g). (c-d) CD-SHG images of the same area in a human cornea transverse sections obtained with elliptically polarized excitations. (e) These elliptical polarizations can be split into circular and linear parts. Collagen structures oriented along the linear part are highlighted in SHG images. (f-g) CD-SHG images of the same area in a human cornea transverse sections obtained with circularly polarized excitations. (h) Perfect circular polarizations: there is no anisotropy in the excitation so no structure is enhanced due to its orientation. The images (d) and (g) were shifted back to -90° in post-processing so that the structures are displayed in the same directions as in (c) and (f) respectively. Scale bar = 20 µm.

This indicates that imperfect circular polarizations of the incident field lead to strong artifacts in the CD-SHG signal: it becomes artificially dependent on the in-plane angle of collagen fibrils, whereas actual CD-SHG signal (with perfect circular polarizations) is expected not to depend on the in-plane orientation. Note that this effect is also observed in conventional optics: linear dichroism can affect the measure of circular dichroism in anisotropic samples.

Similarly, the sensitivity of SHG to sample anisotropy explains the in-plane dependence of artifactual CD-SHG : SHG signal is stronger (resp. smaller) when excited by a linear polarization aligned along (resp. perpendicular to) collagen fibrils, as it has been largely shown with P-SHG [6–13]. Therefore, an elliptical LCP (resp. RCP) field oriented along collagen fibrils will result in an artifactual positive (resp. negative) CD-SHG signal, since CD-SHG is proportional to $I_L^{2\omega} - I_R^{2\omega}$. In the measurements depicted in Fig. 1(c), the elliptical LCP presumably has its linear part oriented at 45° from the y-axis, *ie* along the collagen fibrils within the lamellae. When the sample is rotated by 90°, the collagen lamellae lie perpendicularly to the LCP axis, minimizing the linear contribution of LCP to the SHG signal, so minimizing $I_L^{2\omega}$ that becomes smaller than $I_R^{2\omega}$. $I_R^{2\omega}$ may moreover be maximized after rotation if the axis of the RCP ellipse is also at 135° from y-axis.

Numerical simulations were performed (see Appendix 1) in order to quantify the distortion of the CD-SHG signal as a function of the ellipticity. The main results are shown in Table 1 and Table 2. They show that RCP and LCP ellipticities must be first very close to 1 and secondly

Optics EXPRESS

very similar to each other either in terms of ellipticity or axis orientation, in order to measure the "true" CD-SHG signal (undistorted signal obtained with perfect circular polarization RCP and LCP).

We therefore assessed possible distortions in our setup by characterizing the incident polarizations at different pixels in the field of view. Our measurements reveal the inhomogeneity of the ellipticity throughout the field of view (see Fig. 2(a)), both for RCP and LCP. The polarizations are almost perfectly circular at the center of the field of view ($e > 0.99$), as expected since they are optimized at this position. However, they become more and more imperfect away from the center, where the incident angles on galvanometric and dichroic mirrors are slightly modified. This would not lead to any dramatic effect in the CD-SHG measurement if the elliptical RCP and LCP had exactly the same ellipticity and same axis. But we notice that the RCP and LCP ellipticities differ for a given pixel in the field of view, and that they present two different ellipse orientations, leading to a non zero axis gap (Fig. 2(b)). Experimentally, we took advantage of the quite homogeneous response from collagen membranes on the whole field of view to highlight this phenomenon: artifactual CD-SHG signal was measured at the edges of the field of view (see Appendix 2).

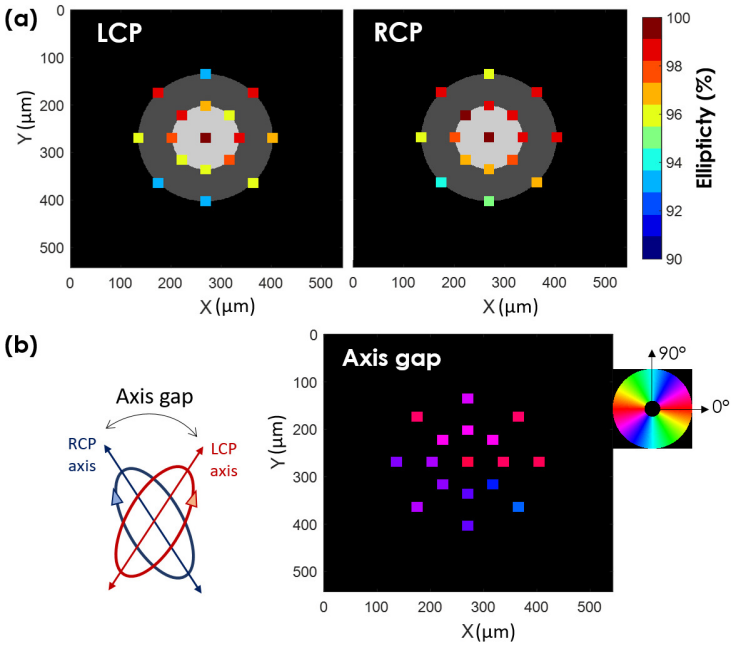

Fig. 2. Polarization characterization in the field of view. (a) Ellipticity (expressed here as a percentage) of the left circular polarization (LCP, left) and the right circular polarization (RCP, right), after optimization. The measurements are taken on 17 pixels throughout the total field of view (540 µm x 540 µm): at the center, on a 135 µm diameter circle (light grey) and on a 270 µm diameter circle (dark grey). (b) Axis gap between the RCP ellipse orientation and LCP ellipse orientation, computed at the same 17 pixels. The gaps lie between 0° and 90 °.

In order to limit the distortion of the CD-SHG signal and to avoid artifactual CD-SHG images affected by linear dichroism, imaging was restricted to central Regions Of Interest (ROIs) with quasi perfect circular polarizations in every pixel. The widest imaging area for our CD-SHG measurements was then 100 µm by 100 µm ($e > 0.96$ for RCP and LCP), and we even performed the majority of measurements in areas of 40 µm by 40 µm ($e > 0.98$ for RCP and LCP).

Optics EXPRESS

3.2. CD-SHG is highly sensitive to noise

In linear optics, circular dichroism (CD) originates in interactions between electric and magnetic dipole moments, which results in a weak signal [29]. In nonlinear optics, CD-SHG may also involve electric and magnetic contributions or purely electric interactions depending on the material [21, 30, 31]. Nevertheless, CD-SHG signal can reach higher values than conventional CD, and published CD-SHG data on collagen span a wide range of values: between 5 % to nearly 100 % depending on the studied tissue [17, 18, 22, 23]. CD-SHG signal is also reported to be non zero only for collagen fibrils lying out of the focal plane [17, 18, 24]. Yet, the SH intensity $I^{2\omega}$ scales as $cos^2(\psi)$, where ψ is the out-of-plane orientation of the collagen fibrils, so it decreases while ψ increases [32]. As a consequence, the CD-SHG signal corresponds to the normalized difference between two low signals, $I_R^{2\omega}(\psi \neq 0)$ and $I_L^{2\omega}(\psi \neq 0)$, and is therefore quite sensitive to the noise. As photon counting is used, a photon noise (shot noise) affects $I_R^{2\omega}$ and $I_L^{2\omega}$: these two intensities are two random variables following Poisson distributions whose parameters $\lambda_{R,L}$ are their respective mean values. The probability to count $I_{R,L}^{2\omega} = n$ photons knowing $\lambda_{R,L} = I_{R,mean}^{2\omega}$ or $I_{L,mean}^{2\omega}$ is written:

$$P(I_{R,L}^{2\omega} = n) = \frac{e^{-\lambda_{R,L}} \lambda_{R,L}^n}{n!} \tag{6}$$

The CD-SHG is thus a combination of such variables. The sum of two Poisson variables with parameters λ_1 and λ_2 follows as well a Poisson distribution with parameter $(\lambda_1 + \lambda_2)$. The CD-SHG is then written as ratios of Poisson variables and consequently its distribution does not have an easy expression [33, 34]. Therefore, we performed numerical simulations to calculate the dispersion of CD-SHG values measured when a Poisson noise affects $I_L^{2\omega}$ and $I_R^{2\omega}$. Theoretical values for the average intensity, $N_{av,th}^{2\omega} = \frac{I_{L,mean}^{2\omega} + I_{R,mean}^{2\omega}}{2}$, and for the CD-SHG, $CD_{th} = \frac{I_{L,mean}^{2\omega} - I_{R,mean}^{2\omega}}{N_{av,th}^{2\omega}}$, that should be measured at one pixel without Poisson noise are set for each simulation. We then derive the Poisson distribution (Eq. 6) of $I_R^{2\omega}$ and $I_L^{2\omega}$ whose parameters are respectively:

$$\begin{aligned} I_{R,mean}^{2\omega} &= N_{av,th}^{2\omega} * \left(1 - \frac{CD_{th}}{2}\right) \\ I_{L,mean}^{2\omega} &= N_{av,th}^{2\omega} * \left(1 + \frac{CD_{th}}{2}\right) \end{aligned} \tag{7}$$

According to these distributions, we generate several pairs $(I_R^{2\omega}, I_L^{2\omega})$ taking Poisson noise into account and calculate the corresponding CD-SHG value and average SH intensity $N_{av}^{2\omega}$. The dispersion of CD-SHG values is shown in Fig. 3. Here, CD_{th} is always set to 0.5 and 100 pairs $(I_R^{2\omega}, I_L^{2\omega})$ are generated for each value of $N_{av,th}^{2\omega}$ ranging from 1 to 100 photons. With these pairs, 10 000 CD-SHG values are computed and plotted against the computed $N_{av}^{2\omega}$ (Fig. 3(a)). Simulations performed with other values of CD_{th} ranging from 0 to 1 gave similar results, indicating that the CD-SHG dispersion does not depend on its central value. We note that CD-SHG dispersion is higher at low average SH intensity $N_{av}^{2\omega}$, and decreases as $\frac{1}{\sqrt{K}}$ when $N_{av}^{2\omega}$ is multiplied by K. In other words, the CD-SHG accuracy increases in the same way as the Signal to Noise Ratio of $(I_L^{2\omega} - I_R^{2\omega})$.

Most importantly, at typical SH intensities obtained during CD-SHG experiments, that is between 10 to 50 photons, the standard deviation of CD-SHG measurements is still quite important, between 0.45 to 0.20 respectively. A higher SH intensity is therefore required to sufficiently improve the accuracy of CD-SHG measurements. Since illuminating the sample with

Optics EXPRESS

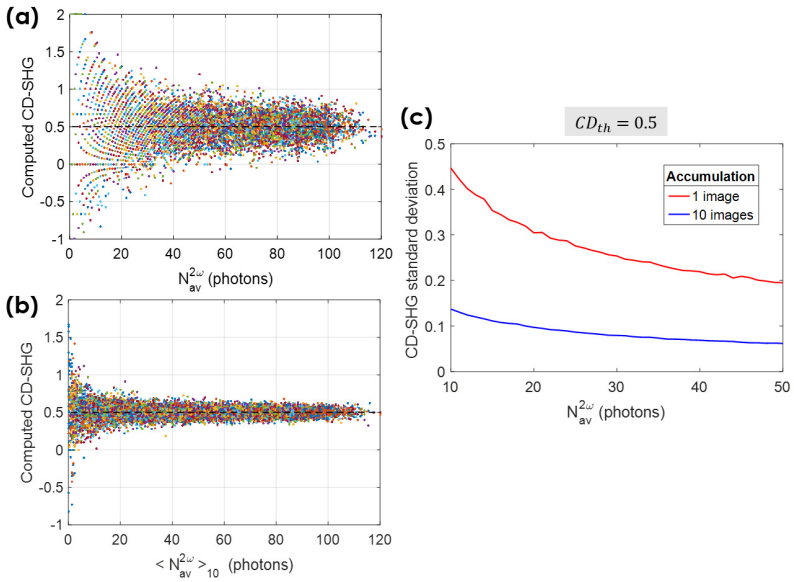

Fig. 3. Dispersion of the CD-SHG values due to Poisson noise affecting $I_R^{2\omega}$ and $I_L^{2\omega}$, as a function of the average SHG signal with or without accumulation. (a) Dispersion scatterplot without accumulation: every point of the scatterplot corresponds to a simulated measure ($N_{av}^{2\omega}$, CD-SHG). (b) Same scatterplot for 10 accumulated values: the measure ($N_{av}^{2\omega}$, CD-SHG) is computed from the average of 10 values of $I_R^{2\omega}$ and $I_L^{2\omega}$ taking Poisson noise into account. (c) Standard deviations of CD-SHG values generated from the theoretical values $CD_{th} = 0.5$ and $N_{av,th}^{2\omega}$ ranging from 10 to 50 photons, without accumulation (in red) and with 10 accumulated values (in blue).

more laser power is not an option due to the damage that high power could cause to biological samples, a way to increase the SH intensity at one point while keeping the sample safe is to accumulate measurements, that is to record the same image several times. Indeed, measurements with accumulation avoid any damage to the sample if they are done in a "time-lapse" mode (with several second breaks between each image) so that the sample can relax between two images. In practice, K RCP (resp. LCP) images are accumulated and average together to obtain a single image with better SNR. The computed CD-SHG is then less dispersed: its dispersion equals the one obtained with an average SH intensity multiplied by K, *ie* it is divided by $\sqrt{K}$. The scatterplot in Fig. 3(b) illustrates the case when 10 images are accumulated: the CD-SHG values are indeed $\sim \sqrt{10}$ times closer to the expected CD_{th} than CD-SHG without accumulation (Fig. 3(a)). The accuracy improvement with time-lapse acquisitions is emphasized in Fig. 3(c) that shows the standard deviation of CD-SHG values obtained with an average SH intensity $N_{av,th}^{2\omega}$ ranging from 10 to 50 photons, when only one image is taken (in red) and when 10 images are accumulated (in blue). The standard deviations drops from [0.20 ; 0.45] in the first case to [0.06 ; 0.14] with 10 accumulated images, which is then sufficient to perform accurate CD-SHG measurements.

3.3. *Time-lapse CD-SHG measurements are sensitive to slight movements*

Time-lapse CD-SHG imaging (*ie* CD-SHG imaging with image accumulation) was used to study collagen fibrils from rat tail tendons, in order to improve the accuracy of the CD-SHG signal. Indeed, a very weak signal is expected from these thin collagen fibrils as the tendon is made quite flat during sample preparation and lies within the focal plane ($\psi \approx 0$).

When accumulating 4 images as shown in Fig. 4, a horizontal drift (toward $x > 0$) of 300

Optics EXPRESS

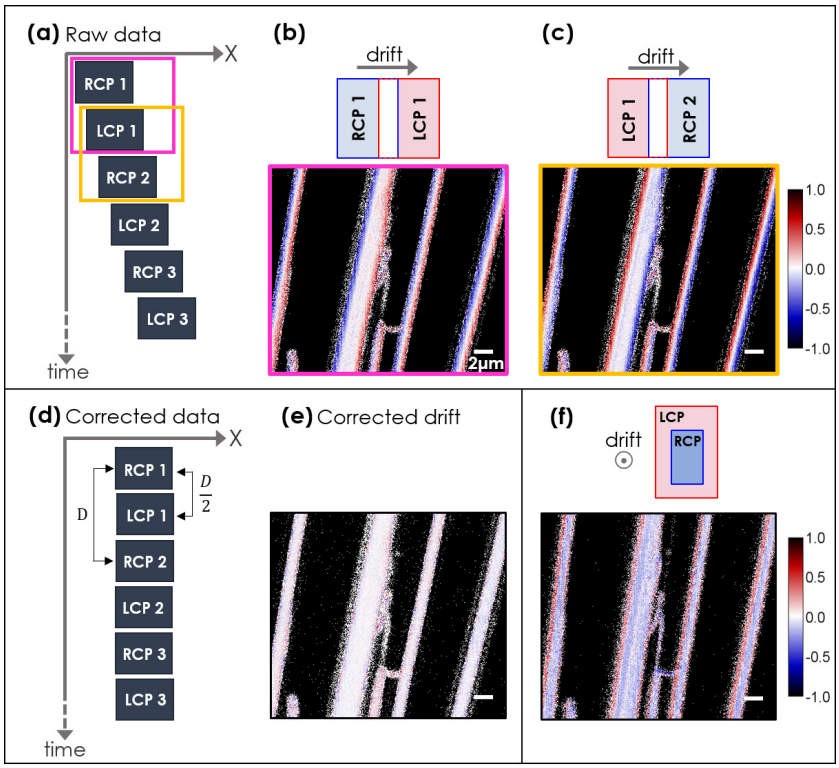

Fig. 4. Effects of lateral (a-c) and axial (f) drifts on CD-SHG signal of collagen fibrils from rat tail tendon. A lateral drift as shown in (a) leads to artifactual strip patterns orthogonal to the drift. The pattern orientation depends on the image chosen as reference for registration: in (b) RCP1 and LCP1 are chosen as references, while in (c) RCP2 and LCP1 are references. A post-processing algorithm is needed to correct for the lateral drift (d) and recover the true CD-SHG signal (e). (f) Axial drift also leads to artifactual CD-SHG signal, and cannot be corrected with simple post-processing. Scale bar = 2 µm.

nm was identified in the RCP image stack as well as in the LCP image stack between the first and the last image, corresponding to a slight drift of approximately 75 nm between each image, *ie* approximately 1 nm/s. Such a small drift is not surprising and is commonly observed in super-resolution imaging. Image registration was thus required before averaging together the RCP, resp. LCP, images. As the 75 nm-drift was not visible between the first two images, two different image registration protocols were performed to verify whether this small lateral drift could affect the CD-SHG signal. The two data processing procedures differed only by the choice of the "reference" image on which the other images were registered before averaging (one has to note that the image acquisition was done in the order illustrated by Fig. 4(a), so that RCP1 and LCP1 were taken successively). First, we chose the first RCP image (referred to as RCP1) and the first LCP image (LCP1) as reference images (Fig. 4(b)). Secondly, we used RCP2 and LCP1 as reference images (Fig. 4(c)). If the lateral drift had no effect on the CD-SHG signal, the two resulting CD-SHG images would have displayed the same patterns. However, we saw that the "blue-white-red" strip pattern from the first processing turned into a "red-white-blue" strip pattern with the second processing. This indicates that the CD-SHG signal was purely artifactual in this case, and that the slight 75 nm-drift created an artificial pattern that could have been misinterpreted as a structural information on collagen fibrils.

Optics EXPRESS

To understand this artifact, one should remember that CD-SHG has the sign of $I_L^{2\omega} - I_R^{2\omega}$ and that the images were sequentially taken in this order: RCP1, then LCP1, then RCP2, and so on. In the case of Fig. 4(b), LCP1 drifted 75 nm to the right from RCP1, so the right part of the strip pattern has a positive CD-SHG signal (red) simply because $I_L^{2\omega} - I_R^{2\omega} = I_L^{2\omega} - 0$ is positive. Similarly, the left part of the strip pattern has a negative CD-SHG signal (blue) as $I_L^{2\omega} - I_R^{2\omega} = 0 - I_R^{2\omega}$ is negative. Similar considerations apply to explain the patterns in Fig. 4(c), considering that RCP2 drifted 75 nm to the right compared to LCP1.

To correct for this lateral drift and measure a non artifactual CD-SHG signal, our data post-processing was improved, assuming the drift to be linear during the whole acquisition, which is a reasonable approximation given the small amplitude of the drift. A basic registration of LCP images on RCP images cannot be used here, as it makes the LCP and RCP structures fully overlaid even though they are truly different, so the CD-SHG signal is artifactually canceled. In contrast, it is possible to register directly the RCP2 image on the RCP1 image, as these two images are expected to show the exact same structures. Thereby, we extracted the drift D that transformed RCP2 image back into RCP1 image. Because LCP1 image was acquired between RCP1 and RCP2, applying half the transformation $\frac{D}{2}$ to LCP1 shifted it back to RCP1 image. Once RCP1 and LCP1 were properly aligned with each other, they could be chosen as reference images to register all the data (Fig. 4(d)). In this case, the true CD-SHG signal appears to be almost zero everywhere (Fig. 4(e)).

To avoid a time-consuming data post-processing, a simple way to minimize the lateral drift is to mechanically stabilize the sample by adding weights on the holder. In our case, the weights consist in a 50 g metal washer. However any addition of weights has to be followed by a sufficient rest period (typically 15 minutes) in order to completely stabilize the stage and avoid any drift in the axial direction that occurs before the holder reaches its equilibrium position. Such an axial drift causes a slight defocus during the acquisition, making the images more and more blurred, so with darker and larger structures. Fig. 4(f) shows the artifactual CD-SHG signal obtained with an axial drift, where the LCP image, acquired after the RCP one, is defocused. The negative (blue) CD-SHG signal in the middle of the fibrils is the consequence of LCP image being less bright than RCP image, and the positive CD-SHG signal (red) at the edges of the fibrils are due to LCP image blurring (leading to image enlargement). An axial drift can also be caused by a capillary attraction between the sample and the objective with water immersion, but addition of weights on the sample holder also addresses this issue.

In practice, this "weight and wait" protocol enables to mechanically stabilize the sample and to perform time-lapse CD-SHG measurements without any mechanical drift.

3.4. Optimized CD-SHG imaging of cornea

Thanks to rigorous artifact controls and corrections (optimization of polarizations and drift minimization), reliable CD-SHG imaging could be done to study collagen structures in human corneas, which present a more complex 3D architecture than tendons. Collagen fibrils in cornea are aligned into stacked lamellae in different en-face orientations, providing a great range of out-of-plane angles when a transverse corneal section is imaged. Single measurements (with no image accumulation) were first performed on a human cornea transverse section and a CD-SHG signal as high as 100 % was extracted (Fig. 5(a)). Time-lapse measurements with 12 accumulated images were then done on the same area (Fig. 5(b). As expected, a better accuracy in CD-SHG is reached with time-lapse measurements. In this CD-SHG image, the alternation of in-plane and out-of-plane lamellae is clearly visualized: the whitest stripes correspond to almost in-plane lamellae while stronger CD-SHG signal corresponds to out-of-plane structures. This is the opposite of the average SH intensity image (~ conventional SHG image), where the in-plane structures are the only ones that provide a fairly good signal. The anti-correlation of the two signals is highlighted in Fig. 5(c) where the average SH intensity image (in green) and the

Optics EXPRESS

absolute value of the CD-SHG image (in magenta) are overlapped. The profile plotted in Fig. 5(d) displays more clearly the signal anti-correlation in the area delimited by the white rectangle in Fig. 5(c). It confirms that CD-SHG signal is weak when SH intensity is maximum (for in-plane collagen structures), and is higher (in absolute value) for structures with a low SH intensity. As a consequence, combining the two modalities allows a great visualization of all the structures constituting the tissue, regardless of their in-plane or out-of-plane orientations.

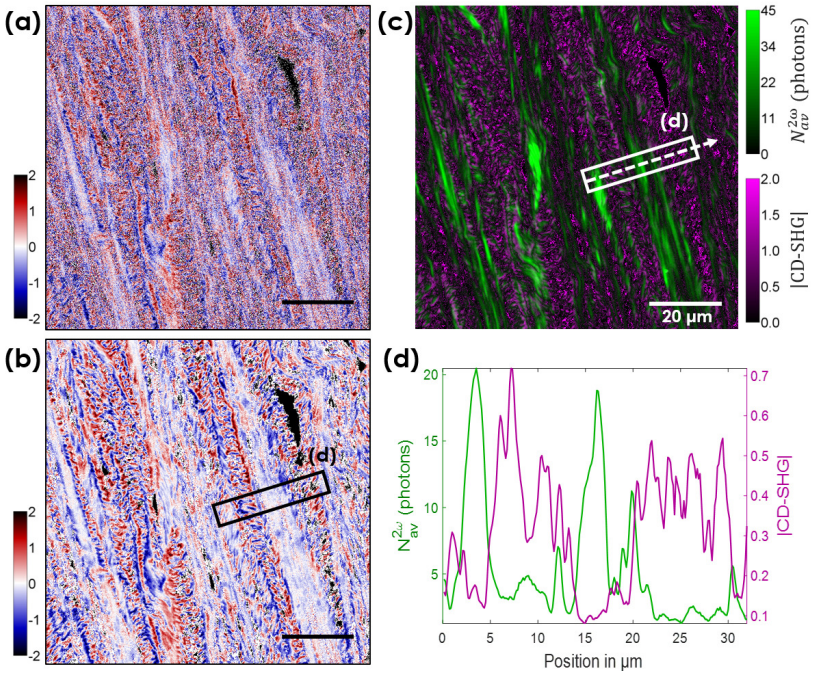

Fig. 5. SHG and CD-SHG imaging of a human cornea transverse section. (a) CD-SHG imaging without image accumulation. (b) CD-SHG imaging with 12 accumulated images. (c) Overlap of the average SH intensity (in green) and the absolute value of CD-SHG (in magenta). (d) Profile plot of the average SH intensity (in green) and CD-SHG absolute value (in magenta) along the white rectangle drawn in (c) (corresponding to the black rectangle drawn in (b)). The values are averaged in the direction perpendicular to the white arrow. Scale bar = 20 µm.

4. Conclusion

This study demonstrates that CD-SHG imaging of collagen is highly sensitive to two types of experimental issues: imperfect circular polarizations and slight movements, regularly encountered in microscopy devices. A weak impairment in ellipticities can lead to strong imaging artifacts in CD-SHG (see Section 3.1) and a slight sample drift, even in the order of the pixel size (a few tens of nanometers), can be detrimental to a correct computation of the CD-SHG (see Section 3.3).

It is crucial to control and remove these artifacts because they may lead to incorrect interpretation of CD-SHG images. This can be done using the protocols described in this paper. First, the ellipticities of RCP and LCP must be controlled by two quarter waveplates to be precisely optimized at the center of the field of view, and then characterized throughout the whole field of view in order to select an imaging area where their values are higher than 0.98. Secondly, sample movement must be avoided as much as possible by mechanical stabilization before each CD-SHG experiment. Other strategies may be used to overcome these slight drift issues, like

Optics EXPRESS

fiducial nano-beads used in super-resolution. For our CD-SHG experiments, the "weight and wait" protocol appears to be sufficient. If necessary, it can be completed by an appropriate post-processing drift correction, provided some conditions: RCP and LCP images are recorded at a regular pace, the drift is small enough to be considered linear during the acquisition, and it belongs to the focal plane only (no axial drift). Another solution might be to implement a fast RCP/LCP switching based on line-to-line (or even pixel-to-pixel) switching of polarization using an electro-optical modulator (EOM), as in [35]. However, as the EOM is located outside the SHG microscope, before galvanometric and dichroic mirrors, a careful calibration may not be sufficient to reach quasi-perfect circular polarizations.

Moreover, as low SHG signals are measured while performing CD-SHG, a strategy of accumulated measurements in a time-lapse mode is proposed in this paper, to improve measurement accuracy. As it extends the acquisition time, the sample drift issue becomes all the more challenging, but can be removed with the same protocol.

The control and correction of all these issues enable the detection of artifact-free CD-SHG signal and allow a reliable study of collagen structure in tissues. We showed that CD-SHG imaging is efficient to visualize the out-of-plane structures in cornea transverse sections and that the combination of this mode of contrast with regular SHG imaging, which highlights fibrils lying in the focal plane, allows the visualization of all fibrils in a tissue, whatever their 3D orientation. Artifact-free CD-SHG imaging therefore appears as a unique technique to explore the 3D organization of tissues.

Appendix 1: Numerical simulations with elliptical polarizations

Numerical simulations were performed with Matlab in order to quantify the distortion of the CD-SHG signal as a function of the ellipticity. For the sake of simplicity, plane wave and electric dipolar approximations were used. The calculation was consistent with previous derivations [17,18] and the values reported in [17] were used for the components of the third-rank susceptibility tensor χ^2:

$$\frac{\chi^{(2)}_{xyy}}{\chi^{(2)}_{xxx}} = 0.63\,, \quad \frac{\chi^{(2)}_{yyx}}{\chi^{(2)}_{xxx}} = 0.48\,, \quad \frac{\chi^{(2)}_{yzx}}{\chi^{(2)}_{xxx}} = -0.14 - 0.19i \tag{8}$$

We first focused on the case where the imperfect RCP and LCP beams have their elliptical polarizations identically oriented (the gap between the major axes of RCP and LCP ellipses is 0°). The main results are displayed in the first column of Table 1 and Table 2: distortions of the CD-SHG signal are computed as the maximum difference between the CD-SHG obtained with imperfect circular polarizations and the "perfect" CD-SHG obtained when $e(RCP) = e(LCP) = 1$, normalized to the perfect CD-SHG. First column of Table 1 shows that the same defect in circularity for both polarizations (that is an identical ellipticity $e < 1$ for RCP and LCP) artifactually reduces the absolute value of CD-SHG, and that this effect increases as the ellipticity decreases. A decrease of 5 % of the CD-SHG signal is found for $e(RCP) = e(LCP) = 0.9$. First column of Table 2 shows that even more dramatic effects occur when RCP and LCP exhibit different ellipticities, even when one of them is close to 1. Here, $e(RCP) = 0.98$ and $e(LCP)$ ranges from 0.82 to 0.98, and a distortion up to 21 % occur in the CD-SHG signal.

Then, because the linear field contributes differently to the SHG depending on its polarization orientation with respect to collagen fibrils, we looked at the distortion of CD-SHG signal when RCP and LCP beams do not have the same ellipse axis of polarization. This leads either to an important increase (when the axis of the LCP ellipse is closer to the collagen fibrils axis than the RCP axis) or decrease (when the RCP axis is closer than LCP axis to the collagen orientation) of the CD-SHG signal. The maximum signal distortion rates are mentioned in the last two columns of Table 1 and Table 2, in the cases of a 45° axis gap and 90° axis gap.

Optics EXPRESS

Table 1. Maximum Distortion of CD-SHG with e(RCP)=e(LCP)

Ellipticity \ Axis gap	0°	45°	90°
1	0 %	0 %	0 %
0.9	5 %	18 %	28 %
0.8	16 %	50 %	69 %
0.7	35 %	95 %	119 %
0.6	64 %	144 %	167 %
0.5	100 %	183 %	201 %

Table 2. Maximum Distortion of CD-SHG with e(RCP)=0.98 and varying e(LCP)

e(LCP) \ Axis gap	0°	45°	90°
0.98	1 %	3 %	5 %
0.94	7 %	9 %	11 %
0.90	13 %	15 %	18 %
0.86	17 %	19 %	22 %
0.82	21 %	23 %	26 %

These simulations raised two points that have to be tackled before CD-SHG imaging: the two circular incident polarizations used to excite the sample must be very similar either in terms of ellipticity or axis orientation, and they must exhibit ellipticities very close to 1. Otherwise, the distortion of CD-SHG signal is too important and imaging artifacts are obtained.

Appendix 2: CD-SHG imaging of collagen membranes

CD-SHG imaging of a collagen membrane, that provides less heterogeneous response than cornea, is presented here to highlight the artifacts that may occur because of inhomogeneities in the incident polarization ellipticities throughout the field of view. Fig. 6 shows the same area of the membrane imaged twice: first when this area is placed at the border of the field of view (Figs. 6(a) and 6(b)) and then when it is centered in the middle of the field of view (Fig. 6(c)). The measured CD-SHG signals differ significantly, which should not be the case if the incident polarization ellipticities were identical throughout the field of view.

Optics EXPRESS

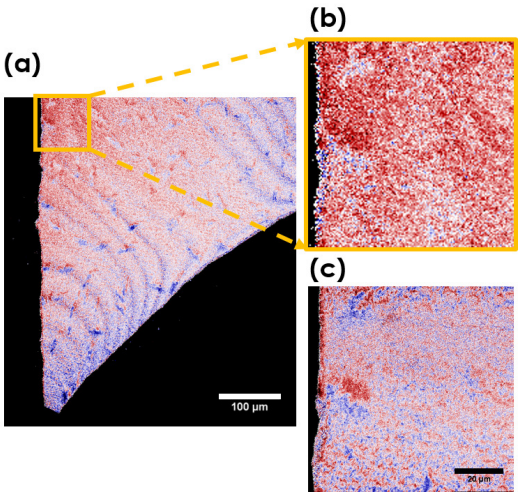

Fig. 6. CD-SHG imaging of a casted collagen membrane. (a) CD-SHG image with a large field-of-view (540 µm x 540 µm). (b) Zoom-in on the yellow rectangle drawn on top of the image in (a). (c) CD-SHG imaging of the exact same area as in (b), after moving the sample to center this area in the middle of the field of view. Scale bar = 20 µm.

Funding

Agence Nationale de la Recherche (ANR) (ANR-10-INBS-04 France BioImaging, ANR-11-EQPX-0029 Morphoscope2).

Acknowledgments

The authors thank Nicolas Olivier, Vincent Maioli and Emmanuel Beaurepaire for helpful scientific discussions, Michèle Savoldelli for human corneas handling, l'Établissement Français du Sang (EFS, Paris) and la Banque Française des Yeux (BFY, Paris) for providing human corneas. M.S. acknowledges financial support from the École Doctorale Interfaces, Univ. Paris-Saclay.

Disclosures

The authors declare that there are no conflicts of interest related to this article.

References

1. D. Hulmes, "Building collagen molecules, fibrils, and suprafibrillar structures," J. Struct. Biol. **137**, 2–10 (2002).
2. K. L. Goh, A. Listrat, and D. Bechet, "Hierarchical mechanics of connective tissues: Integrating insights from nano to macroscopic studies," J. Biomed. Nanotechnol. **10**, 2464–2507 (2014).
3. P. Fratzl and R. Weinkamer, "Nature's hierarchical materials," Prog. Mater. Sci. **52**, 1263–1334 (2007).
4. X. Y. Chen, O. Nadiarynkh, S. Plotnikov, and P. J. Campagnola, "Second harmonic generation microscopy for quantitative analysis of collagen fibrillar structure," Nat. Protoc. **7**, 654–669 (2012).
5. S. Bancelin, C. Aimé, I. Gusachenko, L. Kowalczuk, G. Latour, T. Coradin, and M.-C. Schanne-Klein, "Determination of collagen fibril size via absolute measurements of second-harmonic generation signals," Nat. Commun. **5** (2014).
6. P. Stoller, K. Reiser, P. Celliers, and A. Rubenchik, "Polarization-modulated second harmonic generation in collagen," Biophys. J. **82**, 3330–3342 (2002).
7. F. Tiaho, G. Recher, and D. Rouède, "Estimation of helical angle of myosin and collagen by second harmonic generation imaging microscopy," Opt. Express **15**, 12286–12295 (2007).
8. A. E. Tuer, M. K. Akens, S. Krouglov, D. Sandkuijl, B. C. Wilson, C. M. Whyne, and V. Barzda, "Hierarchical model of fibrillar collagen organization for interpreting the second-order susceptibility tensors in biological tissue," Biophys. J. **103**, 2093–2105 (2012).
9. I. Gusachenko, V. Tran, Y. Goulam Houssen, J.-M. Allain, and M.-C. Schanne-Klein, "Polarization-resolved second-harmonic generation in tendon upon mechanical stretching," Biophys. J. **102**, 2220–9 (2012).

Optics EXPRESS

10. J. Duboisset, D. Ait-Belkacem, M. Roche, H. Rigneault, and S. Brasselet, "Generic model of the molecular orientational distribution probed by polarization-resolved second-harmonic generation," Phys. Rev. A **85**, 043829 (2012).
11. C. P. Brown, M. A. Houle, K. Popov, M. Nicklaus, C.-A. Couture, M. Laliberté, T. Brabec, A. Ruediger, A. J. Carr, A. J. Price, H. S. Gill, L. Ramunno, and F. Légaré, "Imaging and modeling collagen architecture from the nano to micro scale," Biomed. Opt. Express **5**, 233–243 (2014).
12. A. Golaraei, L. Kontenis, R. Cisek, D. Tokarz, S. J. Done, B. C. Wilson, and V. Barzda, "Changes of collagen ultrastructure in breast cancer tissue determined by second-harmonic generation double stokes-mueller polarimetric microscopy," Biomed. Opt. Express **7**, 4054–4068 (2016).
13. A. Benoit, G. Latour, M.-C. Schanne-Klein, and J.-M. Allain, "Simultaneous microstructural and mechanical characterization of human corneas at increasing pressure," J. Mech. Behav. Biomed. Mater. **60**, 93–105 (2016).
14. M. Rivard, C.-A. Couture, A. K. Miri, M. Laliberté, A. Bertrand-Grenier, L. Mongeau, and F. Légaré, "Imaging the bipolarity of myosin filaments with Interferometric Second Harmonic Generation microscopy," Biom. Opt. Express **4**, 2078–86 (2013).
15. M. Rivard, K. Popov, C.-A. Couture, M. Laliberté, A. Bertrand-Grenier, F. Martin, H. Pépin, C. P. Pfeffer, C. Brown, L. Ramunno, and F. Légaré, "Imaging the noncentrosymmetric structural organization of tendon with Interferometric Second Harmonic Generation microscopy," J. Biophotonics **7**, 638–646 (2014).
16. C.-A. Couture, S. Bancelin, J. Van der Kolk, K. Popov, M. Rivard, K. Légaré, G. Martel, H. Richard, C. Brown, S. Laverty, L. Ramunno, and F. Légaré, "The Impact of Collagen Fibril Polarity on Second Harmonic Generation Microscopy," Biophys. J. **109**, 2501–10 (2015).
17. H. Lee, M. J. Huttunen, K. J. Hsu, M. Partanen, G. Y. Zhuo, M. Kauranen, and S.-W. Chu, "Chiral imaging of collagen by second-harmonic generation circular dichroism," Biomed. Opt. Express **4**, 909–16 (2013).
18. G. Y. Zhuo, M. Y. Chen, C. Y. Yeh, C. L. Guo, and F. J. Kao, "Fast determination of three-dimensional fibril orientation of type-I collagen via macroscopic chirality," Appl. Phys. Lett. **110**, 023702 (2017).
19. T. P. Petralli-Mallow, T. M. Wong, J. D. Byers, H. I. Yee, and J. M. Hicks, "Circular dichroism spectroscopy at interfaces: a surface second harmonic generation study," J. Phys. Chem. **97**, 1383–1388 (1993).
20. M. Kauranen, S. Verbiest, J. J. Maki, and A. Persoons, "Second-harmonic generation from chiral surfaces," J. Chem. Phys. **101**, 8193–8199 (1994).
21. A.-M. Pena, T. Boulesteix, T. Dartigalongue, and M.-C. Schanne-Klein, "Chiroptical effects in the second harmonic signal of collagens I and IV," J. Am. Chem. Soc. **127**, 10314–10322 (2005).
22. X. Chen, C. Raggio, and P. J. Campagnola, "Second-harmonic generation circular dichroism studies of osteogenesis imperfecta," Opt. Lett. **37**, 3837–9 (2012).
23. K. R. Campbell and P. J. Campagnola, "Wavelength-Dependent Second Harmonic Generation Circular Dichroism for Differentiation of Col I and Col Ill Isoforms in Stromal Models of Ovarian Cancer Based on Intrinsic Chirality Differences," J. Phys. Chem. B **121**, 1749–1757 (2017).
24. A. Golaraei, M. K. Akens, V. Barzda, K. Mirsanaye, B. C. Wilson, Y. Ro, and S. Krouglov, "Collagen chirality and three-dimensional orientation studied with polarimetric second-harmonic generation microscopy," J. Biophotonics **12**, e201800241 (2018).
25. F. Gobeaux, G. Mosser, A. Anglo, P. Panine, P. Davidson, M.-M. Giraud-Guille, and E. Belamie, "Fibrillogenesis in dense collagen solutions: A physicochemical study," J. Mol. Biol. **376**, 1509 – 1522 (2008).
26. I. Bergman and R. Loxley, "Two improved and simplified methods for the spectrophotometric determination of hydroxyproline," Anal. Chem. **35**, 1961–1965 (1963).
27. C. Teulon, I. Gusachenko, G. Latour, and M.-C. Schanne-Klein, "Theoretical , numerical and experimental study of geometrical parameters that affect anisotropy measurements in polarization-resolved SHG microscopy," Opt. Express **23**, 10168–10176 (2015).
28. P. Mahou, G. Malkinson, É. Chaudan, T. Gacoin, E. Beaurepaire, and W. Supatto, "Metrology of multiphoton microscopes using second harmonic generation nanoprobes," Small **13**, 1701442 (2017).
29. L. D. Barron, *Molecular Light Scattering and Optical Activity* (Cambridge University, 2004), 2nd ed.
30. M. Kauranen, J. J. Maki, T. Verbiest, S. Van Elshocht, and A. Persoons, "Quantitative determination of electric and magnetic second-order susceptibility tensors of chiral surfaces," Phys. Rev. B **55**, R1985–R1988 (1997).
31. F. Hache, H. Mesnil, and M.-C. Schanne-Klein, "Application of classical models of chirality to surface second harmonic generation," J. Chem. Phys. **115**, 6707–6715 (2001).
32. C. Teulon, A. Tidu, F. Portier, G. Mosser, and M.-C. Schanne-Klein, "Probing the 3D structure of cornea-like collagen liquid crystals with polarization-resolved SHG microscopy," Opt. Express **24**, 16084–16098 (2016).
33. J. J. Gart, "The Analysis of Ratios and Cross-Product Ratios of Poisson Variates with Application to Incidence Rates," Commun. Stat. - Theory Methods **7**, 917–937 (1978).
34. T. F. Griffin, "Distribution of the ratio of two poisson random variables," Master thesis, Texas Tech University, USA (1992).
35. G. Ducourthial, J.-s. Affagard, M. Schmeltz, X. Solinas, M. Lopez-Poncelas, C. Bonod-Bidaud, R. Rubio-Amador, F. Ruggiero, J.-M. Allain, E. Beaurepaire *et al.*, "Monitoring dynamic collagen reorganization during skin stretching with fast polarization-resolved second harmonic generation imaging," J. Biophotonics **12**, e201800336 (2019).